

**ARMY RESEARCH LABORATORY**



## **Mesoscale Modeling of Dynamic Failure of Ceramic Polycrystals**

**by J. D. Clayton and R. H. Kraft**

**ARL-RP-328**

**August 2011**

A reprint from the *Proceedings of the 35th International Conference on Advanced Ceramics and Composites*,  
Daytona Beach, FL, 23–28 January 2011

## **NOTICES**

### **Disclaimers**

The findings in this report are not to be construed as an official Department of the Army position unless so designated by other authorized documents.

Citation of manufacturer's or trade names does not constitute an official endorsement or approval of the use thereof.

Destroy this report when it is no longer needed. Do not return it to the originator.

# **Army Research Laboratory**

Aberdeen Proving Ground, MD 21005-5069

---

**ARL-RP-328**

**August 2011**

---

## **Mesoscale Modeling of Dynamic Failure of Ceramic Polycrystals**

**J. D. Clayton and R. H. Kraft**  
**Weapons and Materials Research Directorate, ARL**

A reprint from the *Proceedings of the 35th International Conference on Advanced Ceramics and Composites*,  
Daytona Beach, FL, 23–28 January 2011

REPORT DOCUMENTATION PAGE			Form Approved OMB No. 0704-0188	
<p>Public reporting burden for this collection of information is estimated to average 1 hour per response, including the time for reviewing instructions, searching existing data sources, gathering and maintaining the data needed, and completing and reviewing the collection information. Send comments regarding this burden estimate or any other aspect of this collection of information, including suggestions for reducing the burden, to Department of Defense, Washington Headquarters Services, Directorate for Information Operations and Reports (0704-0188), 1215 Jefferson Davis Highway, Suite 1204, Arlington, VA 22202-4302. Respondents should be aware that notwithstanding any other provision of law, no person shall be subject to any penalty for failing to comply with a collection of information if it does not display a currently valid OMB control number.</p> <p><b>PLEASE DO NOT RETURN YOUR FORM TO THE ABOVE ADDRESS.</b></p>				
1. REPORT DATE (DD-MM-YYYY) August 2011	2. REPORT TYPE Reprint	3. DATES COVERED (From - To) January 2010–January 2011		
4. TITLE AND SUBTITLE  Mesoscale Modeling of Dynamic Failure of Ceramic Polycrystals			5a. CONTRACT NUMBER	
			5b. GRANT NUMBER	
			5c. PROGRAM ELEMENT NUMBER	
6. AUTHOR(S)  J. D. Clayton and R. H. Kraft			5d. PROJECT NUMBER AH80	
			5e. TASK NUMBER	
			5f. WORK UNIT NUMBER	
7. PERFORMING ORGANIZATION NAME(S) AND ADDRESS(ES)  U.S. Army Research Laboratory ATTN: RDRL-WMP-B Aberdeen Proving Ground, MD 21005-5069			8. PERFORMING ORGANIZATION REPORT NUMBER  ARL-RP-328	
9. SPONSORING/MONITORING AGENCY NAME(S) AND ADDRESS(ES)			10. SPONSOR/MONITOR'S ACRONYM(S)	
			11. SPONSOR/MONITOR'S REPORT NUMBER(S)	
12. DISTRIBUTION/AVAILABILITY STATEMENT  Approved for public release; distribution is unlimited.				
13. SUPPLEMENTARY NOTES  A reprint from the <i>Proceedings of the 35th International Conference on Advanced Ceramics and Composites</i> , Daytona Beach, FL, 23–28 January 2011.				
14. ABSTRACT  Mesoscale models are used to study dynamic deformation and failure in silicon carbide (SiC) and aluminum oxynitride (AlON) polycrystals. Elastic and anisotropic elastic-plastic crystal models represent mechanical behavior of SiC and AlON and grains, respectively. Cohesive zone models represent intergranular fracture. Failure data that can be used to inform macroscopic continuum models of ceramic behavior are collected and analyzed. Studied are effects of grain morphology, specimen size, and applied stress state on behavior of polycrystalline aggregates loaded dynamically at applied strain rates on the order of $10^5$ /s. Results for SiC demonstrate shear-induced dilatation, increasing shear strength with increasing confinement or pressure, increasing strength with decreasing specimen size (in terms of number of grains), and decreasing strength variability with decreasing size. Results for AlON demonstrate increased initiation of slip activity—particularly in the vicinity of constrained grain boundaries—with confinement.				
15. SUBJECT TERMS  mesoscale, ceramics, elasticity, plasticity, fracture, defects, SiC, AlON				
16. SECURITY CLASSIFICATION OF:  a. REPORT Unclassified		17. LIMITATION OF ABSTRACT  UU	18. NUMBER OF PAGES  18	19a. NAME OF RESPONSIBLE PERSON J. D. Clayton
b. ABSTRACT Unclassified	c. THIS PAGE Unclassified			19b. TELEPHONE NUMBER (Include area code) 410-278-6146

# MESOSCALE MODELING OF DYNAMIC FAILURE OF CERAMIC POLYCRYSTALS

J.D. Clayton  
U.S. Army Research Laboratory  
RDRL-WMP-B  
Aberdeen Proving Ground, MD 21005-5066  
USA  
john.d.clayton1@us.army.mil

R.H. Kraft  
U.S. Army Research Laboratory  
RDRL-WMP-B  
Aberdeen Proving Ground, MD 21005-5066  
USA  
reuben.kraft@us.army.mil

## ABSTRACT

Mesoscale models are used to study dynamic deformation and failure in silicon carbide (SiC) and aluminum oxynitride (AlON) polycrystals. Elastic and anisotropic elastic-plastic crystal models represent mechanical behavior of SiC and AlON and grains, respectively. Cohesive zone models represent intergranular fracture. Failure data that can be used to inform macroscopic continuum models of ceramic behavior are collected and analyzed. Studied are effects of grain morphology, specimen size, and applied stress state on behavior of polycrystalline aggregates loaded dynamically at applied strain rates on the order of  $10^5/\text{s}$ . Results for SiC demonstrate shear-induced dilatation, increasing shear strength with increasing confinement or pressure, increasing strength with decreasing specimen size (in terms of number of grains), and decreasing strength variability with decreasing size. Results for AlON demonstrate increased initiation of slip activity—particularly in the vicinity of constrained grain boundaries—with confinement.

## 1. INTRODUCTION

Ballistic performance of a ceramic depends on a number of factors associated with the material response to high loading rates and high pressures that arise during impact <sup>1-3</sup>. The performance difference of two monolithic ceramic materials of comparable mass density necessarily originates from microstructure: crystal structure and composition, grain morphology, grain boundaries, and defects such as pores, inclusions, and secondary phases. Crystal structure and composition affect bulk mechanical properties such as elastic stiffness, hardness, cleavage strength, dislocation slip resistance, twinning resistance, and possible phase transformations. Grain boundaries and defects can affect failure properties such as fracture toughness and spall strength.

Mesoscale modeling, wherein geometries of individual grains are resolved explicitly, offers insight into effects of microstructure on dynamic performance of polycrystalline solids. Previous modeling efforts on ceramics have often considered only two spatial dimensions <sup>4-6</sup>. The present representation is three-dimensional, extending work of Kraft et al. <sup>7</sup> and Gazonas et al. <sup>8</sup>. In addition to AlON addressed previously <sup>7, 8</sup>, the present work considers SiC (specifically SiC-N, primarily consisting of the 6H polytype). AlON and SiC exhibit some noteworthy physical differences. SiC ( $\alpha$ -phase, 6H) belongs to a hexagonal crystal system, while AlON ( $\gamma$ -phase) is cubic. Polycrystalline SiC is opaque, while polycrystalline AlON is transparent. SiC has a lower mass density and higher fracture strength and toughness than AlON, with a typical grain size smaller than that of AlON by a factor of ~40. Upon optical examination, AlON <sup>9</sup> appears to have fewer processing defects (e.g., voids and

inclusions) than SiC-N<sup>10</sup>. Both can exhibit limited plasticity under loading involving confining pressure: SiC by propagation of partial dislocations (and associated stacking faults) on {0001} basal planes<sup>11, 12</sup>, and AlON by glide of partial dislocations on {111} octahedral planes<sup>13, 14</sup>.

In addition to providing insight of effects of microstructure on performance, mesoscale modeling can yield information to motivate or parameterize macroscopic models that do not explicitly resolve features of the microstructure. Brittle materials are known to exhibit a size effect, wherein smaller samples are often stronger, typically assumed a result of a lower probability of containment of a critical flaw. Numerical failure modeling of brittle materials is also prone to mesh sensitivity. One representative macroscopic model that addresses issues of failure statistics and size effects is Kayenta<sup>15, 16</sup>. Statistics gathered from mesoscale computations can provide input to Kayenta failure surfaces. Mesoscale simulations can address small specimen sizes comparable to finite element sizes used in macroscopic representations, and can consider homogeneous boundary conditions not easily applied in standard characterization tests for failure of brittle materials. Limitations of the present approach are that polycrystalline samples comparable in size to those tested experimentally cannot be simulated directly due to computing constraints (particularly for SiC with its small grain size) so that validation of mesoscopic computations becomes difficult. Furthermore, a number of microscopic properties are not known precisely (e.g., grain boundary fracture properties), and their effects on macroscopic response must be estimated through extensive parameter studies<sup>4-6, 17</sup>.

This paper is organized as follows. Section 2 summarizes constitutive models for bulk behavior of single crystals of SiC and AlON. Section 3 summarizes fracture models for interfaces. Section 4 discusses microstructures represented in mesoscale finite element simulations of ceramic polycrystals. Sections 5 and 6 report on results for SiC and AlON, respectively. Section 7 concludes the paper.

## 2. CERAMIC SINGLE CRYSTALS: CONSTITUTIVE MODELING

Principles of continuum mechanics are used to represent mechanical behavior of individual grains within a ceramic polycrystal. Notational conventions of nonlinear continuum mechanics<sup>18</sup> are used, with all vectors and tensors referred to a single fixed Cartesian coordinate system. Thermal effects are not considered. Local balances of mass, linear momentum, angular momentum, and energy are

$$\rho_0 = \rho J, \nabla \cdot \mathbf{P} = \rho_0 \ddot{\mathbf{x}}, \mathbf{P} \mathbf{F}^T = \mathbf{F} \mathbf{P}^T, \dot{W} = \mathbf{P} : \dot{\mathbf{F}}, \quad (1)$$

where  $\rho_0$  is the reference mass density,  $\mathbf{F} = \nabla \mathbf{x} = \mathbf{I} + \nabla \mathbf{u}$  is the deformation gradient,  $\nabla$  is the referential gradient operator,  $\mathbf{I}$  is the unit tensor,  $\mathbf{x}(X, t) = \mathbf{X} + \mathbf{u}$  are spatial coordinates with  $\mathbf{u}$  the displacement,  $J = \det \mathbf{F}$ ,  $\mathbf{P}$  is the first Piola-Kirchhoff stress, and  $W$  is the energy density. The deformation gradient and plastic velocity gradient can be written, respectively, as

$$\mathbf{F} = \mathbf{F}^E \mathbf{F}^P, \mathbf{F}^P \dot{\mathbf{F}}^{P^{-1}} = \sum_i \dot{\gamma}^i \mathbf{s}^i \otimes \mathbf{m}^i, \quad (2)$$

where  $\mathbf{F}^E$  accounts for elasticity and rigid rotation,  $\mathbf{F}^P$  accounts for plastic slip, and  $\dot{\gamma}^i$ ,  $\mathbf{s}^i$ , and  $\mathbf{m}^i$  are the slip rate, slip direction, and slip plane normal for slip system  $i$ . Relations in (2) can be extended to account for deformation twins<sup>14, 19, 20</sup> that may be of importance in AlON<sup>9</sup>; discussion of twinning models is omitted here for brevity. Internal energy density is

$$W = \hat{W}(\mathbf{E}^E) + f(\xi), \mathbf{E}^E = (1/2)(\mathbf{F}^{ET} \mathbf{F}^E - \mathbf{I}), \quad (3)$$

where  $\hat{W}$  depends on elastic strain  $\mathbf{E}^E$  via second-order elastic constants and possibly higher-order elastic coefficients or pressure-sensitive second-order coefficients. Stress  $\mathbf{P}$  and Cauchy pressure  $p$  are

$$\mathbf{P} = \mathbf{F}^E (\partial W / \partial \mathbf{E}^E) \mathbf{F}^{P-T}, p = -[1/(3J)] \text{tr}(\mathbf{F} \mathbf{P}^T). \quad (4)$$

In (3), function  $f$  accounts for contributions from defects such as dislocations, vacancies, stacking faults, and twin boundaries, and  $\xi$  is a generic internal state variable representing such defects. In the

absence of slip or defects, and when pressure dependence of elastic coefficients is omitted, (3)-(4) become the usual relations of a Kirchhoff-St. Venant hyperelastic solid with second-order moduli  $\mathbf{C}$ :

$$W = (1/2)\mathbf{E} : \mathbf{C} : \mathbf{E}, \quad \mathbf{E} = (1/2)(\mathbf{F}^T \mathbf{F} - \mathbf{I}), \quad \mathbf{P} = \partial W / \partial \mathbf{F} = \mathbf{F}(\partial W / \partial \mathbf{E}) = \mathbf{F}(\mathbf{C} : \mathbf{E}). \quad (5)$$

In the geometrically linear approximation, (5) is replaced with the familiar linear elasticity relations

$$W = (1/2)\boldsymbol{\varepsilon} : \mathbf{C} : \boldsymbol{\varepsilon}, \quad \boldsymbol{\varepsilon} = (1/2)[\nabla \mathbf{u} + (\nabla \mathbf{u})^T], \quad \mathbf{P} = \mathbf{P}^T = \partial W / \partial \boldsymbol{\varepsilon} = \mathbf{C} : \boldsymbol{\varepsilon} = \mathbf{C} : \nabla \mathbf{u}. \quad (6)$$

Kinetic equations for slip and possible strain hardening are of the functional form

$$\dot{\gamma}^i = \dot{\gamma}^i(\tau^i / \tau_c), \quad \tau_c / G = g(\xi), \quad \dot{\xi} = \dot{\xi}(\dot{\gamma}^i), \quad (7)$$

with  $\tau^i$  the resolved Kirchhoff stress on shear system  $i$ ,  $\tau_c$  the shear strength that is assumed equal for all slip systems,  $G$  the shear modulus that can depend on pressure, and  $g$  a scalar function of dislocation density. More detailed forms of (7) are available elsewhere<sup>14, 19, 20</sup>.

Mechanical properties are listed in Table 1 for the two ceramics studied in the present work. Supporting references with extensive lists of properties are available for SiC<sup>12</sup> and AlON<sup>14</sup>. Cubic elastic constants for AlON are available only from first-principles calculations<sup>7, 8, 21</sup> and are subject to uncertainty, since values quoted have not been validated through experiments. Properties of SiC are representative of SiC-N manufactured by BAE<sup>3</sup>. Properties of AlON are representative of a standard composition having 35.7 mol % AlN<sup>22</sup>. Single crystals are elastically anisotropic; listed bulk and shear moduli and their pressure derivatives at the reference state are representative values for fully dense polycrystals. The initial dynamic slip resistance  $\tau_c$ , in each material approximately 2% of effective shear modulus  $G$ , reflects the experimentally measured polycrystalline shear strength under impact conditions at or above the HEL (strain rate  $\sim 10^5$ /s, pressure  $> 10$  GPa)<sup>11, 14, 23</sup>.

Table 1: Bulk mechanical properties of SiC and AlON

Property	SiC	AlON
Structure	6H	spinel
Phase	$\alpha$	$\gamma$
Crystal system	hexagonal	cubic
Mass density $\rho_0$	3227 kg/m <sup>3</sup>	3714 kg/m <sup>3</sup>
Elastic constant $C_{11}$	501 GPa	377 GPa
Elastic constant $C_{12}$	112 GPa	133 GPa
Elastic constant $C_{44}$	161 GPa	125 GPa
Elastic constant $C_{13}$	52 GPa	(= $C_{12}$ )
Elastic constant $C_{33}$	549 GPa	(= $C_{11}$ )
Bulk modulus $B$	222 GPa	214 GPa
Shear modulus $G$	194 GPa	124 GPa
$B' = dB/dp$	3.10	4.20
$G' = dG/dp$	0.90	0.95
Primary slip plane	{0001}	{111}
Strength $\tau_c/G$	0.022	0.019
Typical grain size	5 $\mu\text{m}$	200 $\mu\text{m}$

### 3. GRAIN BOUNDARY INTERFACES: FRACTURE MODELING

A cohesive zone model is used to represent intergranular (i.e. grain boundary) fracture. First consider mode I fracture. Crack opening initiates when resolved normal traction  $\sigma$  on an interface exceeds fracture strength  $\sigma_c$ . A simple cohesive law of the following form<sup>7, 8</sup> then relates crack opening displacement  $\delta$  and normal traction  $\sigma$ :

$$\sigma = \sigma_c (1 - \delta / \delta_c) \quad [\text{for } 0 < \delta / \delta_c < 1]; \quad \sigma = 0 \quad [\text{for } \delta / \delta_c \geq 1]. \quad (8)$$

In the context of linear elastic fracture mechanics, fracture toughness  $K_c$ , surface energy  $\Gamma_c$ , strain energy release rate  $G_c$ , strength  $\sigma_c$ , critical separation  $\delta_c$ , and cohesive zone length  $l_c$  are related by <sup>17, 24</sup>

$$K_c^2(1-\nu^2)/E = 2\Gamma_c = G_c = (1/2)\sigma_c\delta_c, \quad l_c = \pi E \Gamma_c / [\sigma_c^2(1-\nu^2)], \quad (9)$$

where elastic modulus  $E = 9BG/(3B+G)$  and Poisson's ratio  $\nu = (3B-2G)/(6B+2G)$ . Properties are listed in Table 2 for SiC <sup>3, 16</sup> and AlON <sup>25</sup>, estimated from flexure strength and static fracture toughness measurements. For comparison, spall strengths of SiC <sup>26</sup> and AlON <sup>27</sup> are also listed in Table 2; spall strength values are comparable to flexure strengths, though spall strengths are known vary considerably with impact pressure. Relations analogous to (8) and (9) are used to describe the relationship between shear traction and tangential crack opening (i.e., mode II/III fracture), with equivalent properties. In the finite element implementation of the fracture model, after complete interfacial separation ( $\delta/\delta_c > 1$ ) occurs, interactions between grains are addressed via a multi-body contact algorithm in the SIERRA software framework <sup>28</sup> that prohibits interpenetration of material. Post-fracture contact is assumed frictionless.

More sophisticated cohesive laws with strength or toughness depending on mode mixity, loading rate, and/or temperature are available, and have been examined in detail elsewhere <sup>17, 24, 29</sup>. Transgranular (i.e., cleavage) fracture within individual grains is not modeled in the present work. The assumption that dynamic fracture occurs predominantly at grain boundaries is appropriate for compositions of SiC (e.g., SiC-N) of present interest that fail statically and dynamically in an intergranular fashion <sup>10, 30</sup> and was followed in a previous mesoscale model of spall fracture in SiC <sup>6</sup>. The assumption that dynamic fracture in AlON occurs predominantly at grain boundaries was used by Kraft et al. <sup>7, 8</sup>, though recovered samples from dynamic compression experiments suggest cleavage occurs on {111} planes <sup>9, 13</sup>. A two-dimensional numerical model of transgranular fracture in alumina has been implemented elsewhere <sup>4</sup>; a three-dimensional capability is unavailable in the finite element software <sup>28</sup> used in the present work for materials of current interest. All grain boundaries within a sample of a given material are assumed to have the same properties <sup>6-8</sup>. Fracture strength and/or toughness distributions are expected to exist in real materials (resulting from lattice misorientation distributions and grain boundary defects) and can affect computed macroscopic mechanical properties and failure statistics <sup>4, 5, 17</sup>. As-processed polycrystalline SiC and AlON contain defects such as limited porosity, second-phase inclusions, and small micro-cracks <sup>10, 22</sup>; explicit incorporation of such defects in mesoscale models will be investigated in future work. The present study focuses on effects of grain morphology, bulk material behavior (e.g., crystal structure, elasticity, and plasticity), applied stress state, and specimen size (i.e., number of grains).

Table 2: Fracture properties of SiC and AlON

Property	SiC	AlON
Fracture strength $\sigma_c$	570 MPa	306 MPa
Fracture toughness $K_c$	5.1 MPa m <sup>1/2</sup>	2.5 MPa m <sup>1/2</sup>
Surface energy $\Gamma_c$	28.1 J/m <sup>2</sup>	9.4 J/m <sup>2</sup>
Critical opening $\delta_c$	0.197 μm	0.122 μm
Cohesive length $l_c$	125.8 μm	104.8 μm
Spall strength $\sigma_s$	0.54 GPa - 1.3 GPa	0.14 GPa - 1.7 GPa

#### 4. MICROSTRUCTURAL REPRESENTATIONS

The procedure for generating grain geometries, employing methods and software developed by Rollett and colleagues <sup>31</sup> is discussed in detail elsewhere <sup>7</sup>. Two finite element meshes, each of a

different microstructure, are considered here, as shown in Figure 1. Pertinent properties of each microstructure are listed in Table 3. Cumulative grain size distributions are shown in Figure 2; microstructure I displays a smaller variation in grain size than microstructure II, with more grains of size closer in size to the average grain size. Microstructure I features larger, more equiaxed grains, of more uniform size. Microstructure II features smaller grains, with more jagged grain boundaries. Microstructure I is deemed qualitatively representative of AlON (large equiaxed grains, smooth clean grain boundaries), while microstructure II is more representative of SiC-N (smaller grains, less uniformity, rough boundaries associated with grain boundary segregants). Mesh refinement is sufficient to fully resolve cohesive lengths and grain boundary surface morphology.

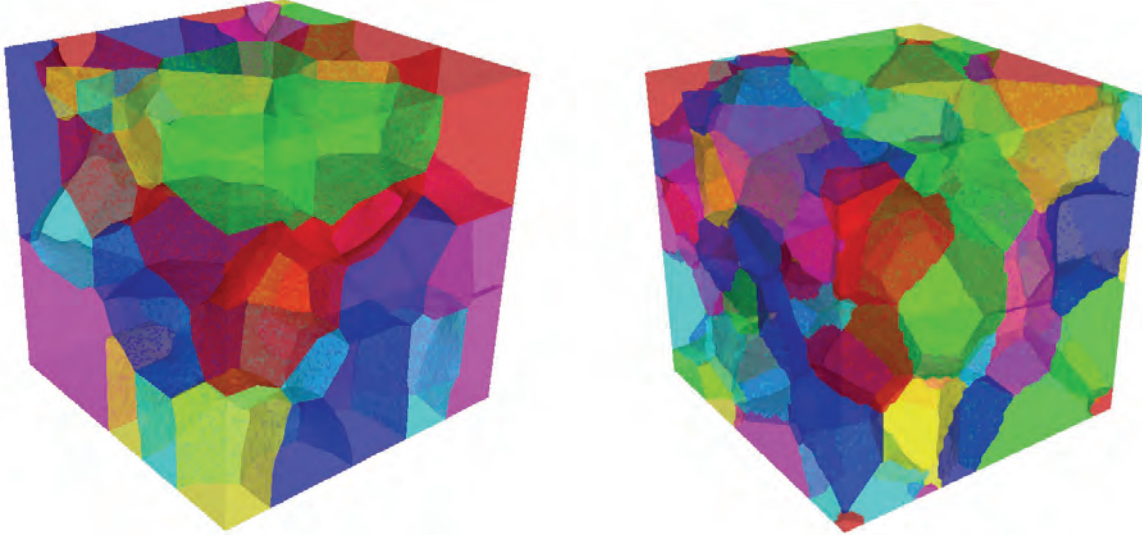


Figure 1: Finite element meshes (left) microstructure I, 50 grains (right) microstructure II, 126 grains [microstructures generated in collaboration with A.D. Rollett, Carnegie Mellon University]

Table 3: Finite element meshes of ceramic microstructures

Microstructure	No. grains	No. elements	Volume [mm <sup>3</sup> ]	Grain boundaries
I	50	1593788	8.0	smooth
II	126	1133743	1.0	rough

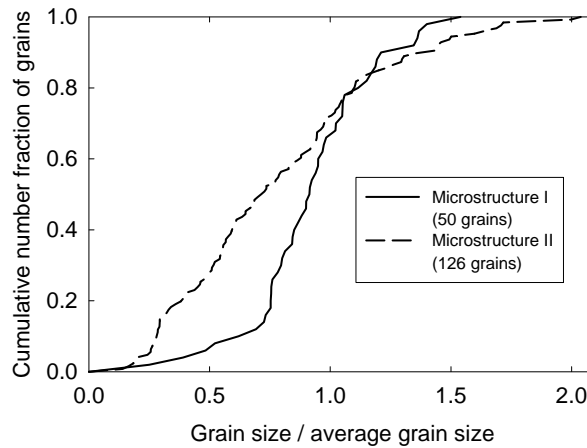


Figure 2: Normalized cumulative grain size distributions

## 5. SILICON CARBIDE: ELASTICITY AND DYNAMIC FRACTURE

A number of simulations using both microstructures (i.e., meshes) listed in Table 3 were conducted using properties of SiC listed in Tables 1 and 2. Simulations of SiC reported here prescribe linear elastic bulk behavior described by (6), with isotropic properties. Boundary conditions are assigned as follows. The microstructure (cube) is fixed along one surface (i.e., one face of the cube), and shear displacement is applied to the opposite face. Lateral sides remain traction-free. One of three additional conditions is simultaneously applied to the sheared face: (i) the face is left free to expand in the normal direction (referred to as free or unconfined shear), (ii) the face is fixed in the normal direction (referred to as fixed or confined shear), or (iii) the face is displaced in the normal direction causing simultaneous compression and shear (referred to as compression + shear). In all cases, the applied shear deformation rate  $\dot{\gamma} = 10^5/\text{s}$ . For compression + shear loading, the applied compressive strain rate is also  $10^5/\text{s}$ . Microstructures are assigned an initial velocity gradient that matches the applied boundary conditions so as to minimize elastic shocks that would arise if nodal velocities were increased from zero in a stepwise manner; however, release waves do originate from traction-free lateral boundaries. Simulations are listed in Table 4; both microstructures are considered. Different simulations for the same microstructure and boundary condition are delineated by shear loading in different directions. For example, forward and reverse loading on one of two orthogonal directions on each of three orthogonal faces of the cube provides up to twelve simulation cases.

Table 4: Numerical simulations of SiC microstructures

Simulation #	Microstructure	Boundary condition
1-4	I	free (unconfined) shear
5-8	I	fixed (confined) shear
9-12	I	compression + shear
13-24	II	free (unconfined) shear
25-36	II	fixed (confined) shear
37-48	II	compression + shear

Representative results from six simulations (one representative of each row in Table 4) are shown in Figure 3. Contours of the shear stress component work conjugate to the loading mode are shown for deformed meshes at an applied shear  $\gamma$  of 5%. Figure legends are truncated to best display the stress distribution; local maxima and minima at stress concentrations may exceed upper and lower bounds of the legends. Displacements are magnified to highlight trends in dynamic fracture behavior. The following results are noteworthy. Stress magnitude tends to increase with increasing confinement, as stress states progress in severity from (a) to (c) to (e) and (b) to (d) to (f). Microstructure I (50 grains) tends to support larger shear stresses, while fractures seem more pronounced for microstructure II (126 grains). For microstructure II, some grains are ejected from the specimen as fragmentation proceeds. For free shear boundary conditions (Figure 3(a) and (b)), shear stresses have relaxed except near a few critical locations at contact surfaces, and significant bending and dilatation are evident along the top (free surface), the latter phenomenon reminiscent of shear-induced porosity described by Shockley et al.<sup>2</sup> and Curran et al.<sup>32</sup>.

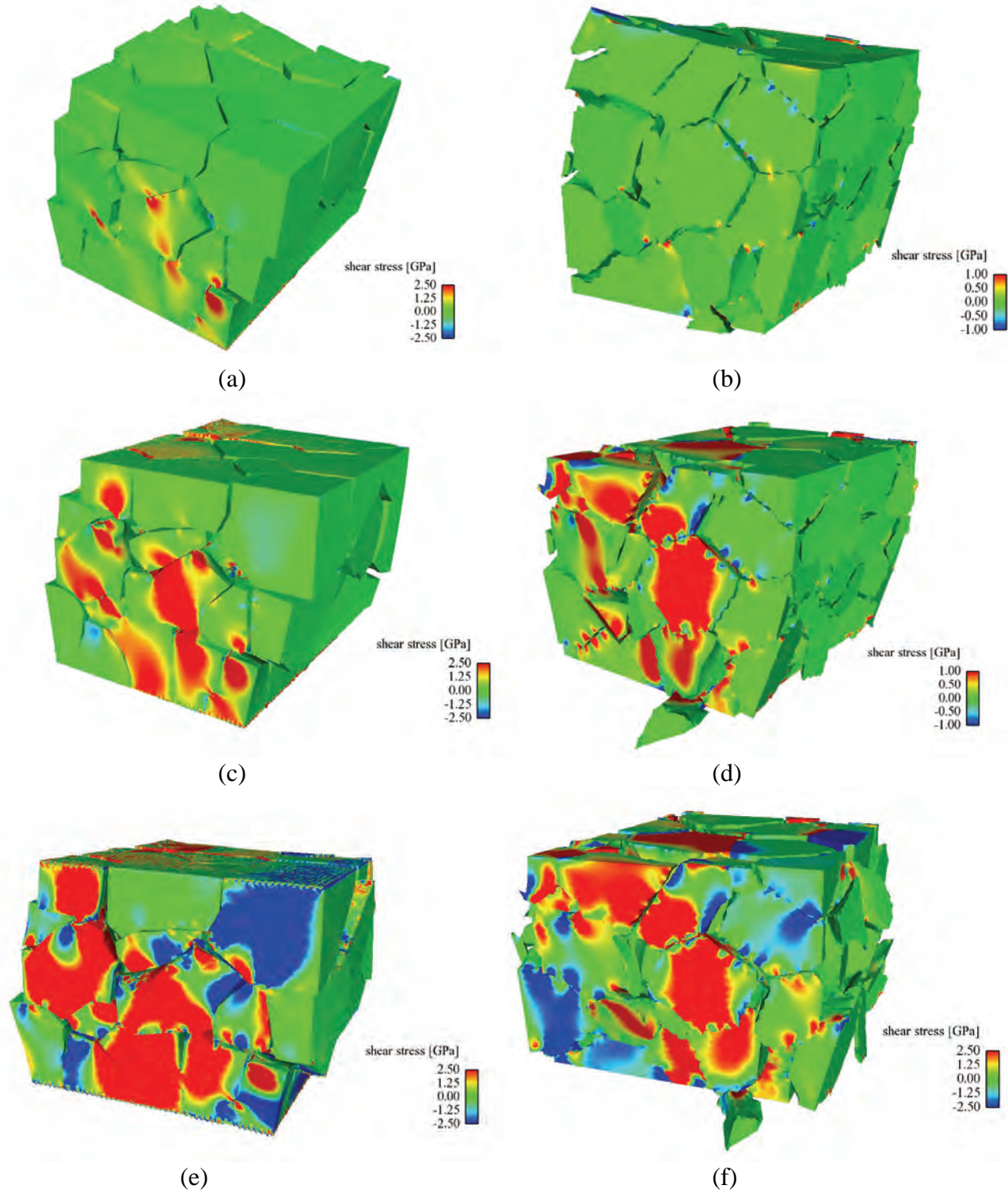


Figure 3: Shear stress in SiC microstructures at applied shear deformation  $\gamma$  of 5%: (a) microstructure I, free shear (b) microstructure II, free shear (c) microstructure I, fixed shear (d) microstructure II, fixed shear (e) microstructure I, compression + shear (f) microstructure II, compression + shear [displacement magnified 5× for (a)-(d); magnified 2× for (e)-(f)]

Figure 4 shows average applied shear stress  $\tau$  and normal stress  $\Sigma$ , obtained from respective nodal reaction forces tangential and normal to the sheared face of the specimen. Results shown correspond to the six cases in Figure 3. Shear strength and normal stress both increase with confinement and further increase with applied compression. Normal stress is negligible for cases corresponding to free shear boundary conditions. Oscillations in shear stress arise as various fracture surfaces are activated, grains slide relative to one another, and sliding is impeded by constraints of neighboring grains or boundary conditions (for cases involving confinement). It is suggested that strength and pressure are greater in microstructure I because fewer, larger grains are favorably oriented for intergranular fracture, and hence fewer fracture sites are available to accommodate the imposed shear deformation. For the same reason, increased dilatation (i.e., bulking) would be expected for samples with fewer, larger grains since crack paths to achieve percolation across whole aggregates would be more tortuous.

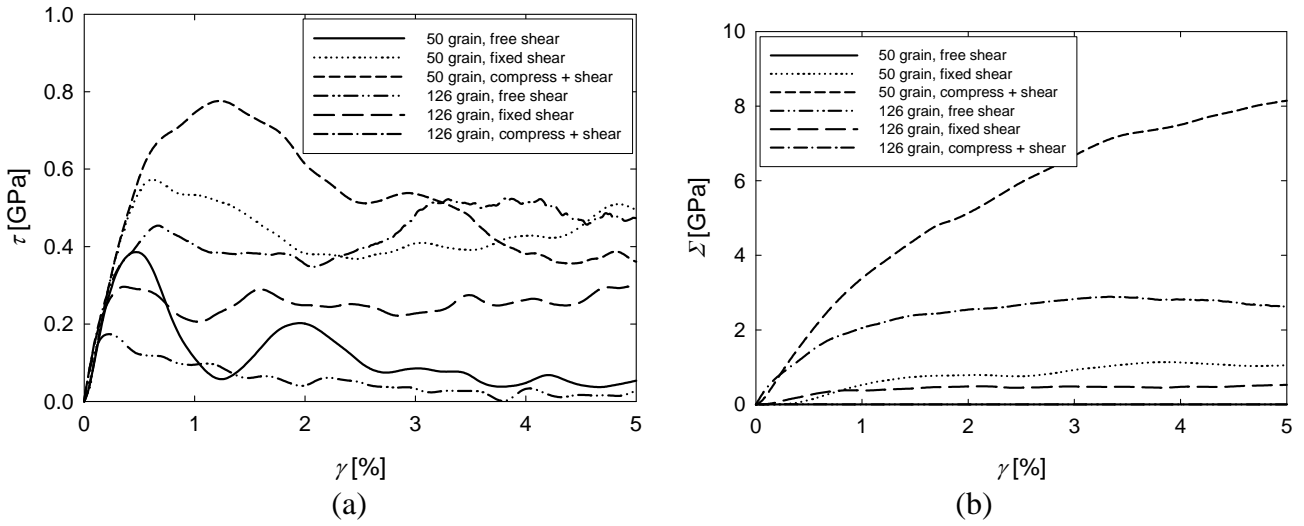


Figure 4: Average shear stress (a) and average normal stress (b) versus applied shear deformation for simulations of SiC microstructures shown in Figure 3

Figure 5(a) shows peak average shear strength  $\sqrt{J_2}$  of each aggregate versus average pressure  $p$ . Results shown are for all simulations in Table 4 for which stable solutions were obtained. The peak shear strength was obtained at an applied strain level corresponding to the first local maxima in the simulation's average  $\tau$ - $\gamma$  curve (e.g., Figure 4(a)), i.e., when  $\partial\tau/\partial\gamma=0$ . Strength is computed via

$$J_2 = (\Sigma^2 + 3\tau^2)/3. \quad (10)$$

For both microstructures, shear strength appears to increase linearly with pressure. Slopes of each linear fit are nearly identical, but the strength intercept at zero pressure is lower for microstructure II. Extrapolation of each curve to null shear provides average hydrostatic tensile strengths of 0.23 GPa and 0.10 GPa for microstructures I and II, respectively. Average strengths can be lower than prescribed cohesive strengths because local fractures initiate and propagate early in the simulations as a result of mixed-mode loading (e.g., combined bending and shear) and inertial effects (e.g., release wave interactions) arising at high loading rates. Though the present results are limited in scope, a decrease in strength with increase in size (measured by number of grains) is apparent from Fig. 5(a). This trend of decreasing strength with increasing size has been reported for static flexure (ring crack) and Hertzian indentation experiments on SiC<sup>33</sup>. The present results suggest that qualitatively similar trends may apply for smaller aggregates of material deformed dynamically at much higher rates.

Figure 5(b) shows peak average strength versus applied shear strain for all cases with free shear boundary conditions (i.e., no confining pressure). Stress relaxation at lateral boundaries and the

cohesive zone-contact model increase the apparent compliance of the aggregate relative to that of an elastic element of material deformed in simple shear (dotted line). Microstructure I (50 grains) exhibits a larger average strength and lower variation in strength (in terms of standard deviation) than microstructure II (126 grains). Static experiments<sup>33</sup> have similarly demonstrated higher characteristic strength and lower variation (i.e., higher Weibull modulus) as the sample size is decreased. Possible correlation between experimentally measured static strength projected to a low failure probability and ballistic performance has been noted<sup>34</sup>; however, correlation of performance with grain size or hardness was not verified in those experiments. The present results suggest that a microstructure containing fewer, larger grains would provide superior dynamic shear strength, with less variation in failure strength, than would a microstructure with smaller, less equiaxed grains, were all other properties (e.g., elastic and interfacial behavior) held fixed. The former class of microstructure would have fewer grain boundary planes favorably oriented for fracture initiation and crack extension and percolation. However, the present computations omit the possibility of grain cleavage. A high purity SiC microstructure with larger grains would be more prone to transgranular fracture than would a microstructure with smaller grains and grain boundary impurities (e.g., SiC-N) that promote crack deflection and toughening<sup>30, 35</sup>.

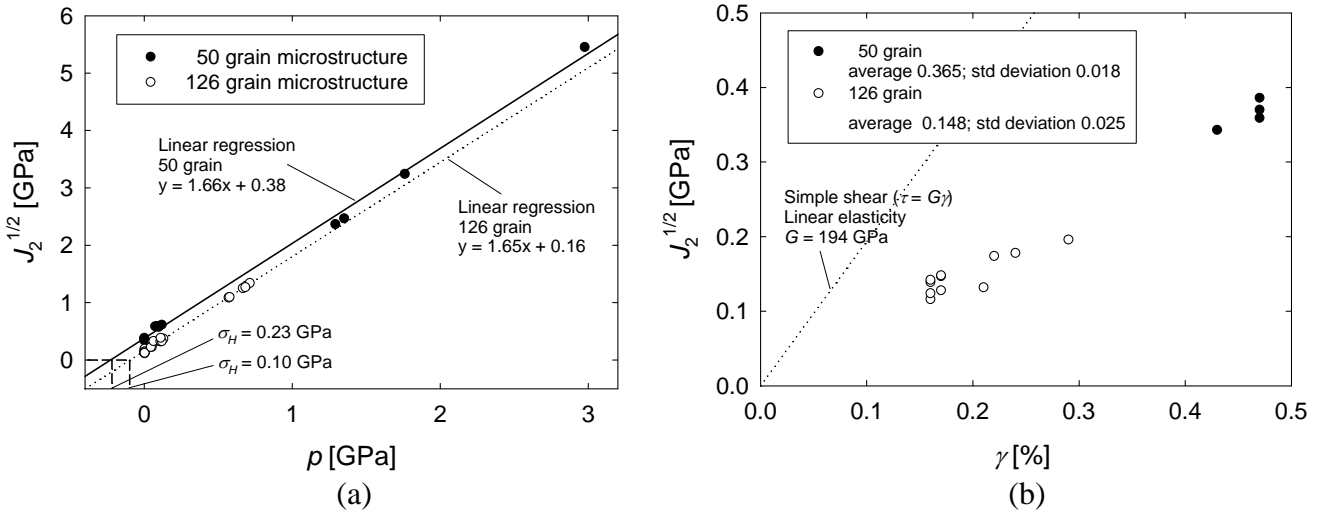


Figure 5: Average peak shear strength versus pressure for all SiC simulations (a) and average peak shear strength versus applied deformation for SiC simulations subjected to free (unconfined) shear (b)

## 6. ALON: ELASTICITY, PLASTICITY, AND DYNAMIC FRACTURE

A geometrically nonlinear anisotropic elastic-plastic model<sup>14</sup> is used to represent behavior of ALON single crystals, corresponding to (2)-(4) and (7) and Tables 1 and 2. The isothermal version of the model used here considers only the primary slip mode:  $\langle 110 \rangle \{111\}$  dislocation glide, with up to twelve active, signed slip systems. Numerical implementation follows Dingreville et al.<sup>36</sup>, modified to account for pressure-dependent cubic elastic coefficients. Results of two simulations are reported, as listed in Table 5. Boundary and initial conditions correspond to those discussed already for SiC polycrystals in Section 5. Stability and computational cost restrict the magnitude of deformation achieved in each simulation to  $\sim 0.5\%$ , which correlates with initiation of plastic yield.

Table 5: Numerical simulations of ALON microstructures

Simulation #	Microstructure	Boundary condition
1	I	free (unconfined) shear
2	I	fixed (confined) shear

Figure 6 shows that increased plastic slip activity—particularly in the vicinity of constrained grain boundaries—occurs in conjunction with confinement associated with fixed shear boundary conditions. Slip initiates due to stress concentrations from intergranular incompatibility (e.g., elastic anisotropy) and contact interactions. Figure 7 shows average shear and normal stresses computed from nodal reaction forces along the sheared (upper) face. Normal stress is negligible for free shear as the upper face is free to expand, but increases in response to bending, nonlinear elasticity (e.g., a Poynting effect<sup>18</sup>), and dilatation resisted by the fixed boundary. Shear stress and pressure for fixed shear loading begin to increase with loading, relative to the free boundary case, as early as 0.2 % shear deformation.

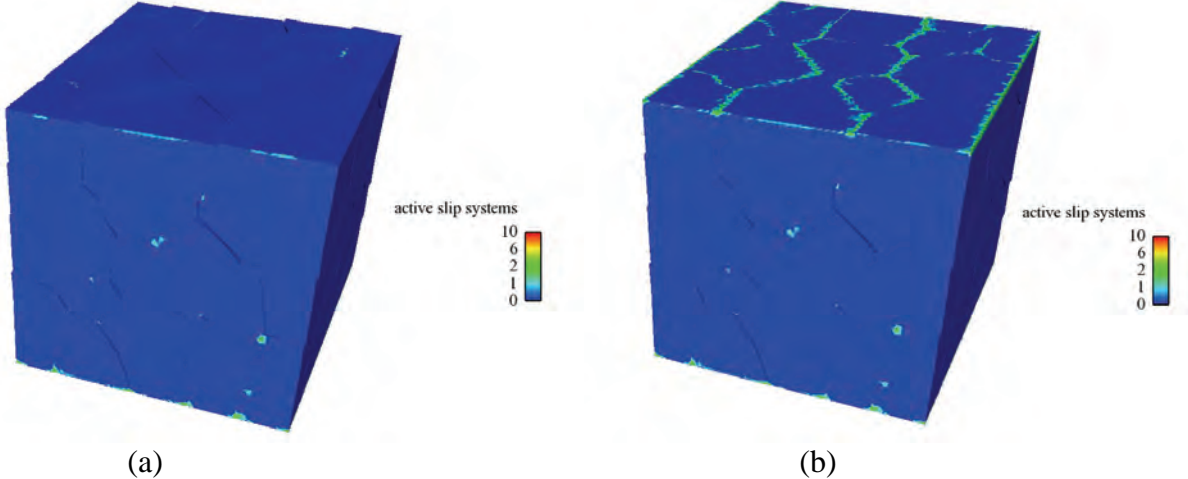


Figure 6: Number of active slip systems in AlON polycrystal deformed under (a) free shear and (b) fixed (confined) shear [shear deformation  $\gamma$  of 0.45%; displacement magnified 20×]

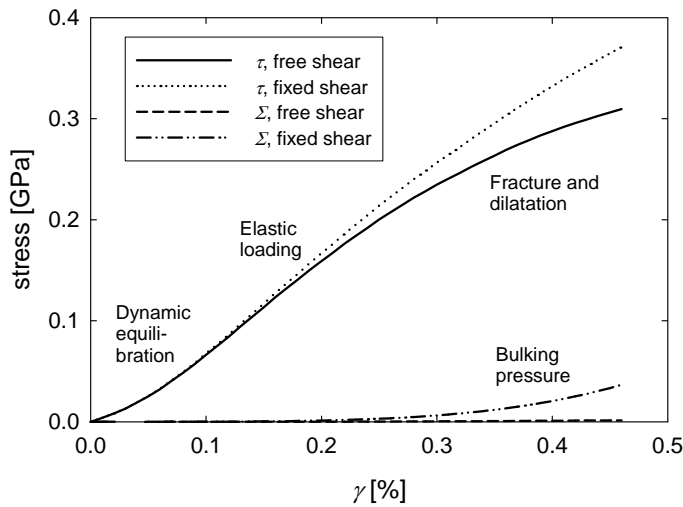


Figure 7: Average shear stress  $\tau$  and normal stress  $\Sigma$  versus shear deformation for AlON polycrystal

## 7. CONCLUSIONS

Mesoscale simulations have been conducted for SiC and AlON polycrystals subjected to high strain rate shear loading ( $10^5/\text{s}$ ) with varying confinement or superposed compression. Results of numerous simulations of SiC, idealized with linear elastic bulk behavior and uniform grain boundary fracture properties, suggest the following trends: (i) shear strength increases linearly with confining pressure and (ii) average shear strength is greater and statistical variation in strength lesser for microstructures with fewer, larger, more uniformly sized grains relative to those with more, smaller,

less uniformly sized grains. Pressure-dependent strength is correlated with shear-induced dilatancy, and such pressure dependence is significant despite the assumption of frictionless post-fracture grain boundary sliding. Variations in failure result only from grain geometry since constitutive properties are uniform. Results of dynamic simulations on AlON demonstrate increased plastic slip initiation with increasing confinement, particularly in the vicinity of grain boundaries along confined surfaces.

## REFERENCES

- <sup>1</sup> J. Sternberg, 1989. Material properties determining the resistance of ceramics to high velocity penetration. *Journal of Applied Physics* 65: 3417-3424.
- <sup>2</sup> D.A. Shockey, A.H. Marchand, S.R. Skaggs, G.E. Cort, M.W. Burkett, R. Parker, 1990. Failure phenomenology of confined ceramic targets and impacting rods. *International Journal of Impact Engineering* 9: 263-275.
- <sup>3</sup> J.C. LaSalvia, J. Campbell, J.J. Swab, J.W. McCauley, 2010. Beyond hardness: ceramics and ceramic-based composites for protection. *JOM* 62, 16-23.
- <sup>4</sup> R.H. Kraft, J.F. Molinari, 2008. A statistical investigation of the effects of grain boundary properties on transgranular fracture. *Acta Materialia* 56: 4739-4749.
- <sup>5</sup> R.H. Kraft, J.F. Molinari, K.T. Ramesh, D.H. Warner, 2008. Computational micromechanics of dynamic compressive loading of a brittle polycrystalline material using a distribution of grain boundary properties. *Journal of the Mechanics and Physics of Solids* 56: 2618-2641.
- <sup>6</sup> J.W. Foulk, T.J. Vogler, 2010. A grain-scale study of spall in brittle materials. *International Journal of Fracture* 163: 225-242.
- <sup>7</sup> R.H. Kraft, I. Batyrev, S. Lee, A.D. Rollett, B. Rice, 2010. Multiscale modeling of armor ceramics. In: J.J. Swab (ed.), *Ceramic Engineering and Science Proceedings: Advances in Ceramic Armor VI*, John Wiley and Sons, Hoboken, NJ, pp. 143-158.
- <sup>8</sup> G.A. Gazonas, J.W. McCauley, R.H. Kraft, B.M. Love, J.D. Clayton, D. Casem, B. Rice, I. Batyrev, N.S. Weingarten, B. Schuster, 2010. Multiscale modeling of armor ceramics: focus on AlON. In: *Proceedings of 27th Army Science Conference*, Orlando, FL, Nov. 29-Dec. 2.
- <sup>9</sup> J.W. McCauley, P. Patel, M. Chen, G. Gilde, E. Strassburger, B. Paliwal, K.T. Ramesh, D.P. Dandekar, 2009. AlON: a brief history of its emergence and evolution. *Journal of the European Ceramic Society* 29: 223-236.
- <sup>10</sup> M.Y. Lee, R.M. Brannon, D.R. Bronowski, 2005. Uniaxial and triaxial compression tests of silicon carbide ceramics under quasi-static loading condition. *SAND 2004-6005*, Sandia National Laboratories, NM.
- <sup>11</sup> D. Zhang, M.S. Wu, R. Feng, 2005. Micromechanical investigation of heterogeneous microplasticity in ceramics deformed under high confining stresses. *Mechanics of Materials* 37: 95-112.
- <sup>12</sup> J.D. Clayton, 2010. Modeling nonlinear electromechanical behavior of shocked silicon carbide. *Journal of Applied Physics* 107: 013520.
- <sup>13</sup> B. Paliwal, K.T. Ramesh, J.W. McCauley, M. Chen, 2008. Dynamic compressive failure of AlON under controlled planar confinement. *Journal of the American Ceramic Society* 91: 3619-3629.
- <sup>14</sup> J.D. Clayton, 2011. A nonlinear thermomechanical model of spinel ceramics applied to aluminum oxynitride (AlON). *Journal of Applied Mechanics* 78: 011013.
- <sup>15</sup> R.M. Brannon, A.F. Fossum, O.E. Strack, 2009. Kayenta: theory and user's guide. *SAND 2009-2282*, Sandia National Laboratories, NM.
- <sup>16</sup> R.B. Leavy, R.M. Brannon, O.E. Strack, 2010. The use of sphere indentation experiments to characterize ceramic damage models. *International Journal of Applied Ceramic Technology* 7: 606-615.
- <sup>17</sup> H.D. Espinosa, P.D. Zavattieri, 2003. A grain level model for the study of failure initiation and evolution in polycrystalline brittle materials. Part I: theory and numerical implementation. *Mechanics of Materials* 35: 333-364.

- <sup>18</sup> A.C. Eringen, 1962. *Nonlinear Theory of Continuous Media*, McGraw-Hill, New York.
- <sup>19</sup> J.D. Clayton, 2009. A continuum description of nonlinear elasticity, slip and twinning, with application to sapphire. *Proceedings of the Royal Society of London A* 465, 307-334.
- <sup>20</sup> J.D. Clayton, 2010. Modeling finite deformations in trigonal ceramic crystals with lattice defects. *International Journal of Plasticity* 26: 1357-1386.
- <sup>21</sup> I.G. Batyrev, B.M. Rice, J.W. McCauley, 2009. First principles calculations of nitrogen atomic position effects on elastic properties of aluminum oxynitride (AlON) spinel. In: *Materials Research Society Fall Meeting*, Boston, MA, Nov. 30-Dec. 1, paper LL5.3.
- <sup>22</sup> E.K. Graham, W.C. Munly, J.W. McCauley, N.D. Corbin, 1988. Elastic properties of polycrystalline aluminum oxynitride spinel and their dependence on pressure, temperature, and composition. *Journal of the American Ceramic Society* 71, 807-812.
- <sup>23</sup> D.P. Dandekar, B.A.M. Vaughan, W.G. Proud, 2007. Shear strength of aluminum oxynitride. In: M. Elert, M.D. Furnish, R. Chau, N. Holmes, J. Nguyen (eds.), *Shock Compression of Condensed Matter 2007*, American Institute of Physics, pp. 505-508.
- <sup>24</sup> J.D. Clayton, 2005. Modeling dynamic plasticity and spall fracture in high density polycrystalline alloys. *International Journal of Solids and Structures* 42: 4613-4640.
- <sup>25</sup> N.D. Corbin, 1989. Aluminum oxynitride spinel: a review. *Journal of the European Ceramic Society* 5: 143-154.
- <sup>26</sup> D.P. Dandekar, P.T. Bartowski, 2001. Spall strengths of silicon carbide under shock loading. In: K.P. Staudhammer, L.E. Murr, M.A. Meyers (eds.), *Fundamental Issues and Applications of Shock-Wave and High-Strain-Rate Phenomena*, Elsevier, New York, pp. 71-77.
- <sup>27</sup> J.U. Cazamias, P.S. Fiske, S.J. Bless, 2001. Shock properties of AlON. In: K.P. Staudhammer, L.E. Murr, M.A. Meyers (eds.), *Fundamental Issues and Applications of Shock-Wave and High-Strain-Rate Phenomena*, Elsevier, New York, pp. 181-188.
- <sup>28</sup> J. Jung, 2010. Presto 4.16 user's guide. SAND 2010-3112, Sandia National Laboratories, NM.
- <sup>29</sup> J.D. Clayton, 2006. Plasticity and spall in high density polycrystals: modeling and simulation. In: M.D. Furnish, M. Elert, T.P. Russell, C.P. White (eds.), *Shock Compression of Condensed Matter 2005*, American Institute of Physics, pp. 311-314.
- <sup>30</sup> C.J. Shih, V.F. Nesterenko, M.A. Meyers, 1998. High-strain-rate deformation and comminution of silicon carbide. *Journal of Applied Physics* 83: 4660-4671.
- <sup>31</sup> A.D. Rollett, P. Manohar, 2004. Monte Carlo modeling of grain growth and recrystallization. In: D. Raabe, F. Roters (eds.), *Continuum Scale Simulation of Engineering Materials*, Wiley, p. 855.
- <sup>32</sup> D.R. Curran, L. Seaman, T. Cooper, D.A. Shockley, 1993. Micromechanical model for comminution and granular flow of brittle material under high strain rate application to penetration of ceramic targets. *International Journal of Impact Engineering* 13: 53-83.
- <sup>33</sup> A.A. Wereszczak, T.P. Kirkland, K.T. Strong, J. Campbell, J.C. LaSalvia, H.T. Miller, 2010. Size-scaling of tensile failure stress in a hot-pressed silicon carbide. *International Journal of Applied Ceramic Technology* 7: 635-642.
- <sup>34</sup> D. Ray, R.M. Flinders, A. Anderson, R.A. Cutler, J. Campbell, J.W. Adams, 2007. Effect of microstructure and mechanical properties on the ballistic performance of SiC-based ceramics. In: L.P. Franks (ed.), *Ceramic Engineering and Science Proceedings: Advances in Ceramic Armor II*, John Wiley and Sons, Hoboken, NJ, pp. 85-96.
- <sup>35</sup> K.T. Faber, A.G. Evans, 1983. Intergranular crack-deflection toughening in silicon carbide. *Journal of the American Ceramic Society* 66: C94-C96.
- <sup>36</sup> R. Dingreville, C.C. Battaile, L.N. Brewer, E.A. Holm, B.L. Boyce, 2010. The effect of microstructural representation on simulations of microplastic ratcheting. *International Journal of Plasticity* 26: 617-633.

NO. OF  
COPIES ORGANIZATION

- 1 DEFENSE TECHNICAL  
(PDF INFORMATION CTR  
only) DTIC OCA  
8725 JOHN J KINGMAN RD  
STE 0944  
FORT BELVOIR VA 22060-6218
- 1 DIRECTOR  
US ARMY RESEARCH LAB  
IMNE ALC HRR  
2800 POWDER MILL RD  
ADELPHI MD 20783-1197
- 1 DIRECTOR  
US ARMY RESEARCH LAB  
RDRL CIO LL  
2800 POWDER MILL RD  
ADELPHI MD 20783-1197
- 1 DIRECTOR  
US ARMY RESEARCH LAB  
RDRL CIO MT  
2800 POWDER MILL RD  
ADELPHI MD 20783-1197
- 1 DIRECTOR  
US ARMY RESEARCH LAB  
RDRL D  
2800 POWDER MILL RD  
ADELPHI MD 20783-1197

NO. OF  
COPIES ORGANIZATION

ABERDEEN PROVING GROUND

52 DIR USARL  
RDRL CIH  
R NAMBURU  
RDRL CIH C  
P CHUNG  
J CLARKE  
D GROVE  
J KNAP  
RDRL WM  
S KARNA  
J MCCUALEY  
P PLOSTINS  
RDRL WMM A  
T WEERASOORIYA  
RDRL WMM B  
G GAZONAS  
D HOPKINS  
B POWERS  
RDRL WMM E  
C HILTON  
J SWAB  
RDRL WMM G  
J ANZELM  
RDRL WML B  
I BATYREV  
B RICE  
N WEINGARTEN  
RDRL WML H  
B SCHUSTER  
RDRL WMP  
S SCHOENFELD  
RDRL WMP B  
R BECKER  
S BILYK  
D CASEM  
J CLAYTON (10 CPS)  
D DANDEKAR  
M GREENFIELD  
C HOPPEL  
Y HUANG  
R KRAFT (5 CPS)  
R LEAVY  
D POWELL  
M RAFTENBERG  
S SATAPATHY  
M SCHEIDLER  
C WILLIAMS  
RDRL WMP C  
T BJORKE  
S SEGLETES

NO. OF  
COPIES ORGANIZATION

RDRL WMP F  
N GNIAZDOWSKI  
RDRL WMP E  
B LOVE